

SOFT X-RAY AND GYRORESONANCE EMISSION ABOVE SUNSPOTS

A. NINDOS¹, M. R. KUNDU, AND S. M. WHITE

Astronomy Department, University of Maryland, College Park, MD 20742

K. SHIBASAKI

Nobeyama Radio Observatory, Minamimaki, Minamisaku, Nagano 384-13, Japan

AND

N. GOPALSWAMY

Department of Physics, Catholic University of America, Washington, DC 20064

Received 2000 March 30; accepted 2000 June 2

ABSTRACT

Using *Yohkoh* SXT and Nobeyama 17 GHz data, we have studied the soft X-ray and microwave emission above several stable, large sunspots near central meridian passage. Our study confirms the well-known fact that soft X-ray emission is depressed above sunspots. It also shows that the distribution of their soft X-ray intensity is not uniform; usually the darkest pixels are associated with the umbra or the far edges of the leading part of the penumbra while the following part of the penumbra may contain higher intensity pixels associated with brighter loops. For the first time, we present a systematic survey of the temperatures and emission measures of the soft X-ray material above sunspots. Sunspots always contain the lowest temperatures and emission measures in the active regions. The mean umbral temperature is 1.8×10^6 K, and the mean penumbral temperature is 2.4×10^6 K. The mean umbral and penumbral emission measures are $\log EM = 26.60 \text{ cm}^{-5}$ and $\log EM = 27.00 \text{ cm}^{-5}$, respectively. The differences between the umbral and penumbral plasma temperatures are physically significant. The higher penumbral values imply that the loops associated with the penumbrae are generally hotter and denser than the loops associated with the umbrae. The highest sunspot temperatures and emission measures are still lower than the average active region parameters but higher than the quiet-Sun plasma parameters. The coronal radiative energy loss rate above the umbrae is 15% higher than the radiative loss rate of the quiet-Sun plasma but a factor of 8.3 lower than the typical active region radiative loss rate. The radio emission comes from the gyroresonance mechanism, and, as expected, it is sensitive to the magnetic field rather than the soft X-ray-emitting plasma.

Subject headings: Sun: corona — Sun: radio radiation — Sun: X-rays, gamma rays

1. INTRODUCTION

Sunspots are associated with the largest concentrations of magnetic field flux in the solar atmosphere. In the photosphere, they consist of two distinct regions that have different photometric and magnetic characteristics. The umbra is the darkest and relatively most homogeneous part of a sunspot and is associated with fields as high as 3000–4000 G. It is cooler than the photosphere by about 2000 K and forms a photometric plateau with a sharp edge independently of its shape. The penumbra contains weaker and more horizontal magnetic fields and has an intermediate brightness. The question of why sunspots are cool has not yet been answered in full detail, but the general idea is that their strong magnetic fields suppress convective energy transport (see Jahn 1992 for a review).

Structures in soft X-ray images of active regions represent coronal density structures and usually outline magnetic field lines. However, the areas directly above sunspots are not usually bright in soft X-rays (Pallavicini et al. 1979; Webb & Zirin 1981). The soft X-ray depletion above sunspots has been confirmed by several studies (e.g., Walker et al. 1988; Golub et al. 1990; Sams, Golub, & Weiss 1992; Harmon et al. 1993). These studies have established that soft X-ray loops avoid the sunspot umbrae. To the best of

our knowledge, no systematic study of the spatial distribution of temperature and emission measure of the X-ray-emitting material above sunspots has been made. Before the launch of the *Yohkoh* satellite, such calculations were not possible because the capabilities of previous soft X-ray telescopes were strongly limited by their sensitivity and by the large amounts of scattered emission from the bright regions adjacent to sunspots, which contaminate the sunspot signal. The soft X-ray imaging telescope (SXT) on board *Yohkoh* (Tsuneta et al. 1991) is a much better instrument for studying the corona above large sunspots because of its increased sensitivity and the better scattering properties of its mirrors. However, scattered light may be a concern even for SXT especially when we study faint structures close to bright sources. The temperatures to which SXT is sensitive depend on the filter combination used. Overall it is most sensitive to hot plasma above 2×10^6 K (see Tsuneta et al. 1991 for the SXT's temperature response curves). The combination of Al.1 and AlMg filters is more sensitive to plasma below 2 MK than combinations that include thicker filters such as the thick Al and Be filters (however, even the sensitivity of the Al.1/AlMg pair below 2.5 MK is reduced compared with its sensitivity at 3 MK).

Sunspot-associated radio sources have also been observed at microwaves for many years (e.g., Kundu et al. 1977). The dominant emission mechanism at microwaves can be gyroresonance (g-r) or free-free depending on the magnetic field strength and frequency. Unlike free-free,

¹ Present address: Section of Astrogeophysics, Physics Department, University of Ioannina, Ioannina GR-45110, Greece.

which has no characteristic frequency, gyroresonance is a resonant mechanism; opacity is significant only in thin layers where the observing frequency is a low-integer multiple of the local electron gyrofrequency (see White & Kundu 1997 for a review of the properties of the g-r mechanism). Gyroresonance can render sources optically thick in the corona and produce brightness temperatures of about 10^6 K. The g-r emission in the extraordinary mode (*e*-mode) comes primarily from the third or lower harmonics of the gyrofrequency, whereas ordinary mode (*o*-mode) emission has less opacity and comes from the second harmonic. On the other hand, free-free emission tends to be weakly polarized and favors low frequencies and/or dense cool plasmas. Model computations (e.g., Gelfreikh & Lubyshv 1979; Alissandrakis, Kundu, & Lantos 1980; Krüger, Hildebrandt, & Fürstenberg 1985; Brosius & Holman 1989; Gopalswamy et al. 1996; Nindos et al. 1996; Vourlidis, Bastian, & Aschwanden 1997; Lee et al. 1998) have confirmed that the primary emission mechanism of microwave sunspot sources is gyroresonance (g-r). The structure of the source depends upon which of the low-order (second to fourth) harmonics of the gyrofrequency are located in the low corona. Observations of gyroresonance sources represent the only means to obtain quantitative information on the magnetic field at different heights of the solar corona. In addition to the magnetic field, g-r emission also depends on plasma temperature and density, but unlike soft X-ray emission its dependence on the plasma parameters is much weaker than its dependence on the magnetic field. Therefore, the determination of temperatures and emission measures of the soft X-ray-emitting plasma above sunspots will complement the information provided by sunspot-associated microwave g-r sources (for a comparison between radio and EUV/X-ray observations see the review by White 1999). Comparisons between observations of g-r sources and the plasma parameters derived from soft X-ray images may have the potential of providing more accurate constraints on coronal magnetic field estimates.

In this paper, we study the coronal atmosphere above the umbrae and penumbrae of several large stable sunspots by combining *Yohkoh* SXT images and Nobeyama Radioheliograph (NoRH) images at 17 GHz. The NoRH radio data have the advantage that well-defined bright g-r sources appear above sunspots at 17 GHz when the magnetic field is strong, the spatial resolution of the data can be about $12''$, images are available every day since 1992, and the data are well calibrated. Additional photospheric white-light images and images of the longitudinal component of the photospheric magnetic field were provided by KPNO. The goal of our study is twofold: (1) to determine accurately the spatial structure of temperature and emission measure of the X-ray-emitting plasma above sunspot umbrae and penumbrae and (2) to check whether the SXT emission measures and temperatures can constrain the parameters needed in modeling sunspot-associated g-r sources.

2. DATA ANALYSIS

From the Solar Geophysical Data Reports, we selected large symmetric sunspots for the period from 1992 April (the month that Nobeyama Radioheliograph began observations) to 1998 June. Their areas were larger than 200 millionths of the visible photospheric disk. The radii of the umbrae and penumbrae in our sample were in the ranges $8''$ – $22''$ and $18''$ – $32''$, respectively. Therefore, our umbrae

and penumbrae contained 8–63 and 42–133 full-frame-image (FFI) SXT pixels, respectively. No big sunspots were present in 1994–1995 because of the solar minimum. Frequent flaring in the vicinity of sunspots complicates the analysis of their soft X-ray and microwave emission because postflare loops may dominate the emission for a long time. The flare productivity of each candidate active region was checked by visual inspection of SXT movies and light curves of the 17 GHz emission. Several large candidate sunspots have not been included in our data set because they were located in flare-productive active regions. Care was taken so that most sunspots of our data set were not located close to the limb because we do not want the plage/loop X-ray emission to either block or contaminate the sunspot emission significantly.

2.1. Soft X-Ray Data

In this study, we used full-frame SXT images (FFIs) obtained with the Al.1 and AlMg filters. Originally, all SXT images were processed with the standard calibration software, which does the data decompression, background subtraction, correction for solar rotation, and coregistration of images.

Since the soft X-ray emission above sunspots is not bright, long-exposure images are needed for the calculation of the sunspot plasma parameters. On the other hand, such images may be affected by saturation in the brighter parts of the active regions or even in parts of the sunspots. Therefore, both long-exposure and short-exposure images must be used for the calculation of the plasma parameters above the whole active region. The order in which we performed the analysis is as follows. (1) In all cases, in order to improve photon statistics, for each filter we summed several SXT images provided that there was no transient brightening activity in the sunspot vicinity. We summed the short-exposure images and long-exposure images separately. After the summation of long-exposure images, the typical exposure times of the resulting Al.1 and AlMg images were about 19 and 37 s, respectively. The corresponding times for the resulting short-exposure Al.1 and AlMg images were 2 and 4.3 s. (2) Composite images were produced by combining the image that resulted from the summation of the long-exposure images with the image that resulted from the summation of the short-exposure images. After exposure normalization we replaced the saturated pixels of the long-exposure image with the corresponding pixels of the short-exposure image. (3) The images from step 2 were used for the computation of temperatures and emission measures (EMs). This was done with the application of the filter ratio method to the Al.1 and AlMg images (e.g., see Hara et al. 1992). In the computation of the emission measures we did not use the Meyer (1985) model of coronal abundances, which has been incorporated in the standard *Yohkoh* software; instead we adopted (see White et al. 2000) an Fe/H abundance in the corona that is 4 times larger than the value given by Meyer (1985). For the two plasma parameters, we also computed the uncertainties associated with random errors due to photon counting statistics and data compression using the formulae given by Klimchuk & Gary (1995). Based on these errors we have ignored all pixels with $d \log EM > 0.25$ and $d \log T_e > 0.07$ in the subsequent analysis. (4) In the cases where the computations showed large error bars over most of the sunspot area, we averaged signals from two pixels of the composite images of step 2 in

order to improve the signal-to-noise ratio and carried out the T_e -EM calculation again. Sometimes this method produced error bars below our thresholds, but in other cases the original error bars were so big that it did not work. The pixel size of the temperature and emission measure maps presented in Figure 1 is $9''.82$ for the 1992 July 12 sunspot, the 1992 August 9 sunspot, and the 1993 February 10 sunspot; all other SXT maps have a pixel size of $4''.91$.

Given that soft X-ray emission is depressed above sunspots, it is very important to evaluate the contribution of the emission from nearby bright loops to the weak sunspot soft X-ray emission. This contribution arises from the fact that the point-spread function (PSF) of the SXT has finite dimensions and obviously is not a delta function. The PSF consists of two components: a core and the immediate wings have been fitted by Martens, Acton, & Lemen (1995) to an elliptical Moffat function, while the far (X-ray scattering) wings beyond about $20''$ from the location of the maximum fall off approximately as the inverse square of the distance (Hara et al. 1994). In order to correct for the contamination of the sunspot signal we must deconvolve the SXT's PSF from each SXT image. We imported SXT images and the corresponding PSF functions into AIPS and deconvolved them using the standard maximum entropy method (AIPS task VTESS). In the cases where the MEM algorithm converged, the intensity of the corrected thin aluminum filter images above the sunspot area was about 29% smaller than in the original thin aluminum filter images. For the sandwich filter image it was somewhat higher (about 35%). Using the corrected images, the derived sunspot temperatures are somewhat lower (about 20%). We note that the MEM algorithm did not converge to a solution in all cases. It did not converge in cases where even the short-exposure images suffered from saturation and hence part of the composite image was also saturated. It also did not work satisfactorily in cases where the soft X-ray morphology of the active region was complicated. In the cases where MEM did not work, we evaluate the scattered light contribution from the far wings of the PSF using the formulae of Hara et al. (1994). In these cases the reduction of intensity above the sunspot is about 16% for the thin aluminum filter images and 22% for the sandwich filter images and the derived temperatures are lower by about 11%. Therefore, the temperatures derived in the cases where only the effect of the far wings of the PSF was removed must be considered as upper limits to the real temperatures. The sunspot emission measure changes for two reasons: (1) the reduced intensity due to the correction of the image and (2) the lower temperature. These two changes have opposite signs and in all cases that we studied we found no significant changes in emission measure before and after deconvolution or scattered light subtraction.

2.2. Temperature and Emission Measure Uncertainties

The sources of uncertainty are as follows.

1. Uncertainties due to photon statistics. Especially in the pixels with very low soft X-ray emission, uncertainties are high and no reliable calculation can be performed. In § 2.1, we described the method we used in order to reduce the uncertainties. In the pixels that contain bright emission, the error bars from the computations that use the composite images are not different from the error bars from the computations that use the short-exposure images. However,

as expected, the error bars above sunspots and regions of weak emission are reduced significantly; in all cases it is impossible to compute sunspot plasma parameters with error bars lower than the thresholds defined in § 2.1 using short-exposure images only. For each sunspot, the final uncertainties (after all steps of data reduction) are presented in Table 1. Without any stray light corrections the temperature uncertainties were higher by about 15%–20% in the cases where MEM algorithm converged and higher by 10%–15% in the cases where only the scattered light due to the effect of the far wings of the PSF was subtracted. The emission measure uncertainties are not affected significantly by the deconvolution or the scattered light subtraction. Porter & Klimchuk (1995) warned that the uncertainties derived by the formulae given by Klimchuk & Gary (1995) must be treated cautiously, especially for nonflaring conditions. For each sunspot of Table 1, we computed the standard deviation of the umbral and penumbral T_e and log EM distributions. The T_e standard deviations were about 8%–12% higher than the errors in Table 1, but the EM standard deviations were 2–2.3 times higher. The differences between the predicted errors and standard deviations are the result of inaccuracies in the error expressions. Therefore, the temperature errors seem fairly accurate, but the real emission measure errors are probably higher than the ones quoted in Table 1.

2. Systematic uncertainties associated with the calibrations of the telescope, detectors, and filters. They depend only on the plasma temperature and not on the observed intensity. Their exact value is not precisely known, but Klimchuk & Gary (1995) give their upper limits. Using their curves, we found that for the range of our sunspot temperatures and emission measures the upper limit of the systematic uncertainties can be as high as 0.05–0.1 and 0.12–0.25 in $\log T$ and $\log EM$, respectively.

3. In the emission measure calculations there is one more source of uncertainty, which comes from the ambiguity of the determination of coronal elemental abundances. Unlike most previous SXT studies, throughout this paper we do not use the Meyer (1985) model, which is the default in the SXT software, but instead we adopt abundances in which Fe is 4 times higher than in the Meyer corona. This modification was done because recently there is enough evidence (see Feldman 1992; White 1999; White et al. 2000; J. Zhang, M. R. Kundu, & S. M. White 2000, in preparation) that in the quiet corona the Fe/H abundance is about 4 times larger than the value given by Meyer (1985). Therefore, when we compare our emission measures with previously published results, we must divide the older values by a factor of 4.

2.3. Radio and Optical Data

The 17 GHz data were obtained with the Nobeyama Radioheliograph (NoRH), which is a large T-shaped array that consists of 84 antennas (Nakajima et al. 1991). The maps in total intensity I and circular polarization V were produced using aperture synthesis techniques. For each day, 2 hr long visibility data sets around local noon were imported into AIPS and mapped using uniform weighting, which yields higher spatial resolution and lower sidelobes than natural weighting at the expense of slightly reduced sensitivity. The maximum entropy method (MEM) was

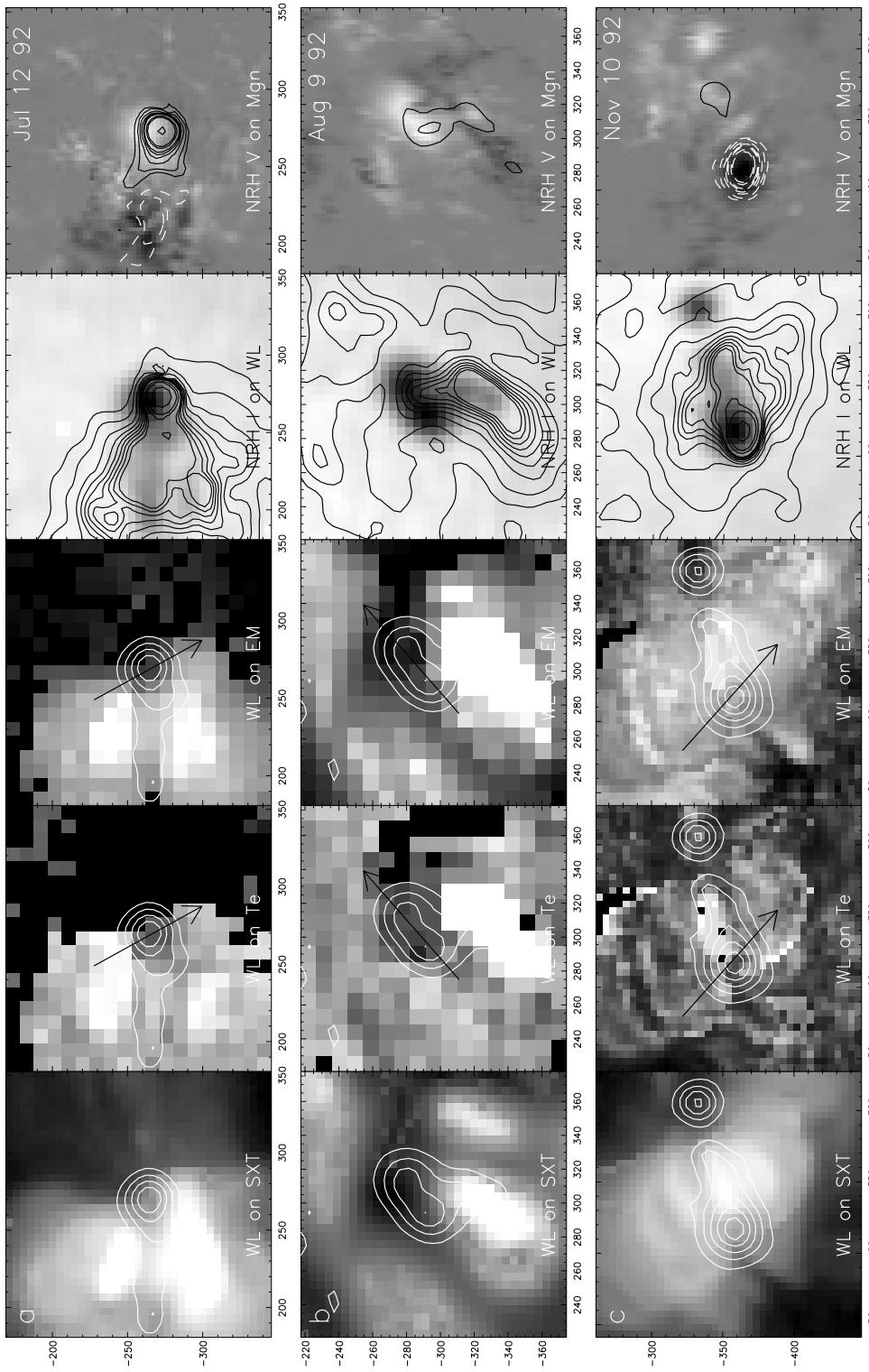


FIG. 1.—*First column*: SXT A1.1 composite image and contours of the white-light sunspot overlaid on the computed temperature and emission measure map, respectively. *Fourth column*: Contours of the 17 GHz I emission overlaid on the white-light image. *Fifth column*: Contour plots of the 17 GHz V emission overlaid on a KPNO magnetogram. The contour levels of the I maps are (12, 15, 20, 25, 30, 35, 40, 45, 50, 75, 100, 200, 400, 600, 900) \times 1000 K, and the contour levels of the V maps are (–700, –500, –300, –100, –80, –50, –40, –30, –20, –10, –5, 5, 10, 20, 30, 40, 50, 80, 100, 300, 500, 700) \times 1000 K. Dashed contours in the V maps denote negative values. *Row a*: 1992 July 12 sunspot of active region (AR) NOAA 7220. *Row b*: 1992 August 9 sunspot of AR NOAA 7248. *Row c*: 1992 November 10 sunspot of AR NOAA 7335. *Row d*: 1992 December 23 sunspot of AR NOAA 7374. *Row e*: 1993 February 10 sunspot of AR 7417. *Row f*: 1993 June 29 sunspot of AR 7529. *Row g*: 1993 July 1 sunspot of AR 7529. *Row h*: 1993 July 22 sunspot of AR 7548. *Row i*: 1993 November 5 sunspot of AR 7613. *Row j*: 1998 June 9 sunspot of AR 8232. The axes denote seconds of arc from the center of the disk. North is up and west is to the right.

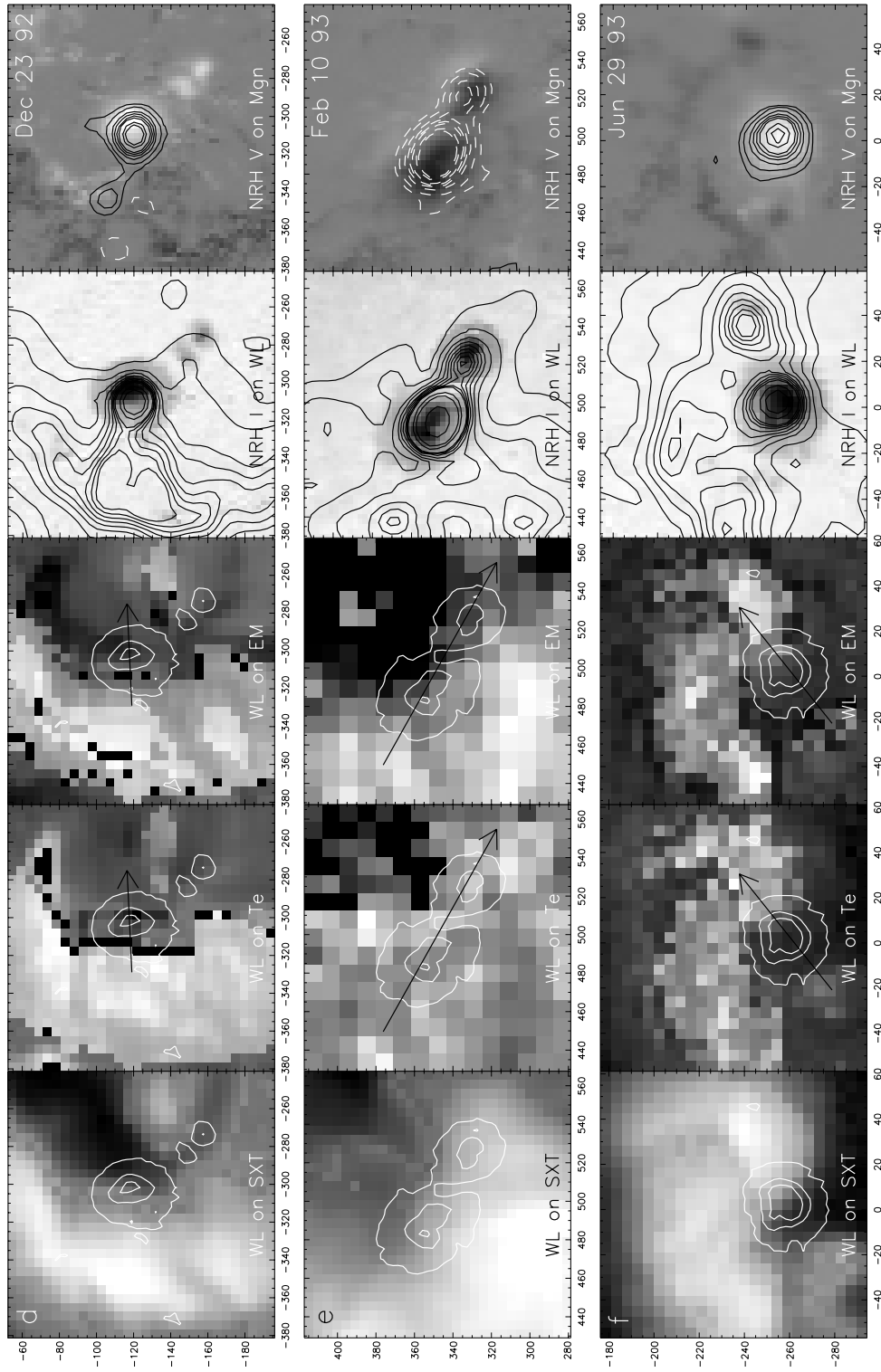


FIG. 1.—Continued

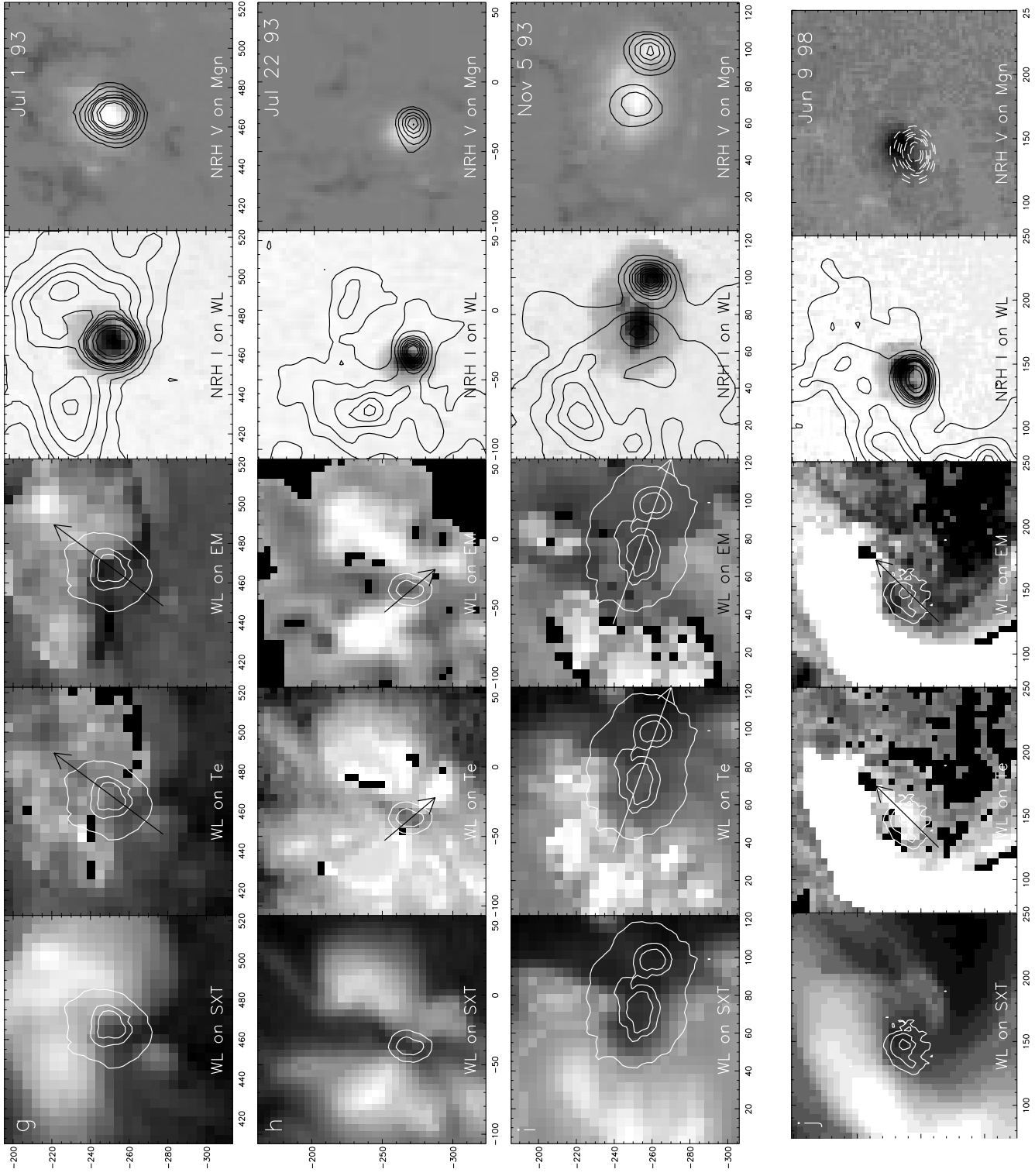


FIG. 1.—Continued

TABLE 1
SOFT X-RAY PLASMA PARAMETERS OF SUNSPOTS

Date	Heliographic Coordinates	T_e^{umbra} ($\times 10^6$ K)	T_e^{penum} ($\times 10^6$ K)	$\log \text{EM}_{\text{umbra}}$ (cm^{-5})	$\log \text{EM}_{\text{penum}}$ (cm^{-5})
1992 Jul 12	S11W03	2.1 ± 0.10	2.8 ± 0.17	26.60 ± 0.10	27.40 ± 0.17
1992 Aug 9	S13W12	1.8 ± 0.14	2.1 ± 0.12	26.68 ± 0.05	26.84 ± 0.11
1992 Nov 10 ^a	S17E20	3.0 ± 0.15	3.6 ± 0.18	27.40 ± 0.10	27.65 ± 0.15
1992 Dec 23	S09E17	1.6 ± 0.16	1.8 ± 0.11	26.78 ± 0.13	26.87 ± 0.16
1993 Feb 10 ^a	N16W15	2.0 ± 0.12	2.1 ± 0.20	26.84 ± 0.12	26.95 ± 0.11
1993 Jun 29	S11W01	1.7 ± 0.11	2.0 ± 0.14	26.72 ± 0.08	26.84 ± 0.14
1993 Jul 1	S13W24	2.3 ± 0.16	3.0 ± 0.20	26.70 ± 0.10	27.18 ± 0.17
1993 Jul 22	S12E07	1.4 ± 0.12	2.9 ± 0.19	26.80 ± 0.08	27.08 ± 0.14
1993 Nov 5	S12E06	1.7 ± 0.13	1.8 ± 0.19	26.60 ± 0.11	26.65 ± 0.16
1998 Jun 9	S21W08	2.7 ± 0.12	2.2 ± 0.15	26.70 ± 0.13	26.52 ± 0.17

NOTE.—In this table and throughout the paper, the emission measures have been computed assuming that the Fe/H abundance in the corona is 4 times larger than the value given by Meyer 1985.

^a Eastern sunspot.

used for the deconvolution of the resulting dirty maps after any bright sources were CLEANed out. The reader may refer to the appendix of the article by Nindos et al. (1999) for details. Here the only difference was that before adding back the CLEAN components of the bright emission, we rotated them to a common time, which was usually the middle of the visibility data set. Our final maps have the advantage of improved $u - v$ coverage from 2 hr long visibilities, which yields maps of higher fidelity, and excellent spatial resolution ($12''$). These improvements yield high-resolution, high dynamic range images, which are crucial in the detection of small localized sources such as the gyroresonance sources at 17 GHz. CLEAN algorithms also perform reasonably well for bright, well-defined sunspot-associated sources (see Nindos et al. 1999 for a detailed comparison between different deconvolution methods applied to NoRH data).

White-light images are used for the identification of the borders of sunspot umbrae and penumbrae. Until 1992 November *Yohkoh* SXT routinely obtained white-light images. For the sunspots that were observed after 1992 November, we used KPNO white-light images. For all sunspots, we also used the KPNO magnetograms, which give the longitudinal component of the photospheric magnetic field.

This research requires very careful coregistration of data obtained at radically different wavelengths. Even in the cases where we averaged SXT signals from 2 pixels for the T_e -EM calculations, we used the composite SXT images before summation for the overlays; therefore, the pixel size of all SXT images used in the overlays was $4''.9$. Our reference time for the coregistrations was the time of the SXT image with the highest contrast. We rotated the Nobeyama images and KPNO images to that time and did the overlays using the known pointing information of the instruments. We note that in a few cases no KPNO images were available the day of SXT/NoRH observations that we analyze. In these cases, we used KPNO images made the previous or following day and rotated them appropriately. Of course, these transformations assume that no major changes occurred in the sunspots. To a first approximation, this assumption is valid because first we checked the NoRH and SXT data for flare activity and we rejected sunspots located at flare-productive or rapidly evolving regions; furthermore, it is known that the boundaries of umbrae and pen-

umbrae of large stable sunspots usually do not change significantly within 24 hr (Zirin 1988). The overlays were also checked by comparing the extended thermal emission, which is visible in soft X-ray and microwave images. The extended thermal emissions were also compared with the plages as were outlined in the photospheric magnetograms. Only in two cases were our overlays unsatisfactory, and in these cases we shifted the images manually to achieve a better match. In all other cases, the agreement was good and we are confident that the accuracy of our overlays is less than about 1 SXT full-frame image pixel ($4''.9$).

3. SOFT X-RAY EMISSION ABOVE SUNSPOTS

Our sample contains 19 sunspots. Here we present only the sunspots where the error bars of the majority of their pixels are $d \log T < 0.07$ or $d \log \text{EM} < 0.25$. In Figure 1, we show the sunspots and the surrounding active regions as they appear in SXT composite images. We also present the temperature and emission measure images that we calculated. Contours of the white-light images that show the borders of the umbra and penumbra have been overlaid on the soft X-ray intensity, temperature, and emission measure images. In the same figures, we also show contour plots of the 17 GHz I emission overlaid on white-light images and contour plots of the 17 GHz V emission overlaid on KPNO magnetograms. Since this is the first systematic quantitative study of the sunspot soft X-ray plasma parameters, in Figure 2 we present selected profiles of the temperatures and emission measures along the lines defined by the arrows that appear in Figure 1.

A first inspection of the soft X-ray images shows that there is a depression in the soft X-ray emission in almost all sunspots that we studied. Using the composite images of the figures, we can measure at the same time the weak sunspot emission and the bright loop emission. The measurements confirm the visual inspection and show that in the Al.1 filter images the average sunspot soft X-ray emission is $15\text{--}190 \text{ DN s}^{-1}$ (1 DN corresponds to a signal of 100 electrons in the CCD of the SXT; see Tsuneta et al. 1991). The darkest sunspots include those for which we cannot derive reliable plasma parameters for the majority of their pixels, and hence they are not presented in the figures. For the sunspots shown in the figures, the average flux is $50\text{--}190 \text{ DN s}^{-1}$. For comparison we note that the average value of the quiet-Sun pixels in the Al.1 images is $10\text{--}50 \text{ DN s}^{-1}$. On the other

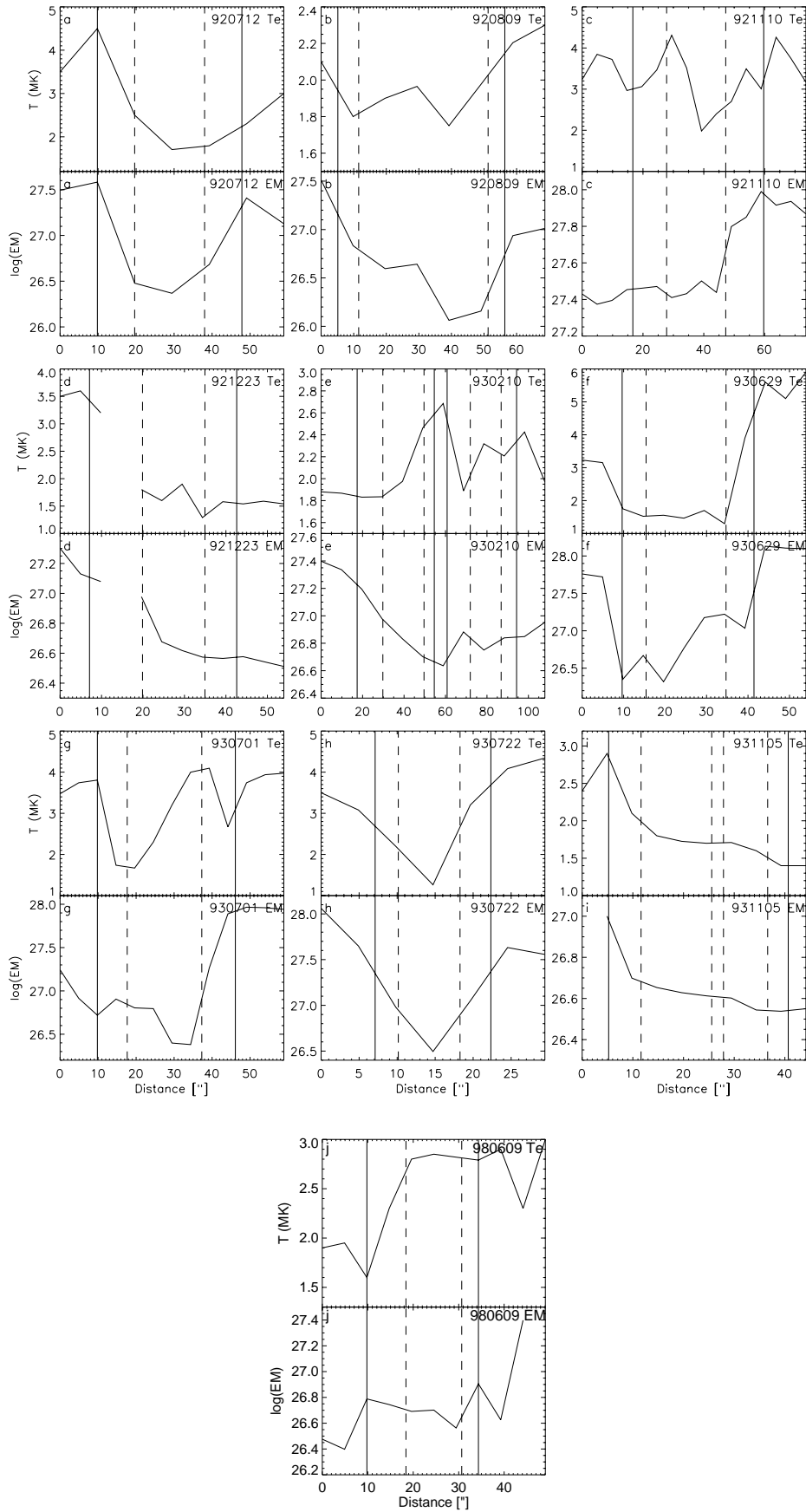


FIG. 2.—Profiles of the temperature and emission measure along the lines defined by the arrows in the temperature and emission measure images of Fig. 1. Profiles along the (a) 1992 July 12 sunspot, (b) 1992 August 9 sunspot, (c) 1992 November 10 sunspot, (d) 1992 December 23 sunspot, (e) 1993 February 10 sunspot, (f) 1993 June 29 sunspot, (g) 1993 July 1 sunspot, (h) 1993 July 22 sunspot, (i) 1993 November 5 sunspot, and (j) 1998 June 9 sunspot are shown. The distance along the lines increases toward the arrowhead. The vertical solid and dashed lines denote the positions of intersection between the arrows of Fig. 1 and the borders of the penumbrae and umbrae, respectively.

hand, the typical emission from the bright soft X-ray loops of the active regions that contain the sunspots is 500–4000 DN s^{-1} . The 1992 November 10 sunspot (see Fig. 1, row c) shows the highest soft X-ray emission (320 DN s^{-1}). The images show that in most cases the distribution of the soft X-ray emission above the sunspots is not uniform. Usually, the highest soft X-ray emission is associated with the following part of the penumbrae and could reach 75–530 DN s^{-1} . This is a direct consequence of the fact that the majority of our sunspots (12 of 19) are located at the leading parts of the active regions; therefore, the emission of the trailing part of the sunspots is influenced by brighter loops even in sunspots that are located close to the center of the disk. The lowest level of the soft X-ray emission is usually associated with the umbra and the leading part of the penumbra, and it is in the range 4–35 DN s^{-1} .

Now let us focus on the computed temperatures and emission measures. In Figure 1, pixels with uncertainties $d \log T > 0.07$ or $d \log \text{EM} > 0.25$ have been blanked out. Also in Figure 1, row b, the southern part of the 1992 August 9 penumbra appears white in the temperature and emission measure maps because the bright loop emission saturated even in the short-exposure images. In the 1998 June 9 images (Fig. 1, row j), the pixels associated with the bright active region soft X-ray emission appear white in the temperature and emission measure map because our calculations were not reliable. The reason was that most of the short-exposure images were taken with exposure times of 17 ms (for the Al.1 filter) and 38 ms (for the AlMg filter) (instead of the usual 78 and 168 ms). We could not sum images that cover more than a 1 hr period because of the occurrence of transient brightenings in the bright part of the active region (that transient activity took place 50" away from the sunspot, however, and did not affect the sunspot area and its vicinity). Figures 1 and 2 show that in most cases (a notable exception is the 1998 June 9 sunspot) the umbrae are among the areas with the lowest temperatures and emission measures in the active regions. Figure 2 shows that sunspots contain pixels with temperatures as low as 1.4 MK and emission measures as low as $\log \text{EM} = 26.2$. The sunspot that shows the highest temperatures and emission measures is the 1992 November 10 trailing sunspot (Fig. 1, row c, and Fig. 2c). Furthermore, Figures 1 and 2 indicate that the temperatures and emission measures show higher inhomogeneity above the penumbrae than above the umbrae.

In Table 1, we present a summary of the results of our analysis. We give the average value of temperature and emission measure above the umbrae and penumbrae separately. The umbral/penumbral borders were defined from the white-light KPNO images: the umbral areas contained pixels with intensities $I_{\text{wl}} < 1000$, and the penumbral areas contained pixels with $2000 < I_{\text{wl}} < 10000$ (in the arbitrary units of the KPNO images). In all cases the calculated borders agreed with the visual inspection of the sunspots. Overall, the umbral plasma parameters appear lower than the penumbral plasma parameters. In each case, we also give the uncertainties. The reader should refer to § 2.2 for a detailed discussion of the T_e -EM uncertainties. The fact that the standard deviations of the temperature distributions are generally consistent with the derived temperature errors indicates that these error bars are reliable and therefore the difference between the umbral and penumbral temperatures is physically significant. On the other hand, such agreement

did not exist for the emission measures, and therefore the quoted emission measure uncertainties may underestimate the real uncertainties.

The different properties of the umbral and penumbral plasma parameters can be more clearly seen in the histograms of Figure 3. The two distinct peaks of the umbral and penumbral distributions can be clearly seen. The mean temperature of all valid umbral pixels is 1.8×10^6 K, and the mean temperature of all valid penumbral pixels is 2.4×10^6 K. The mean emission measure of all valid umbral pixels is $\log \text{EM} = 26.60 \text{ cm}^{-5}$, and the mean emission measure of all valid penumbral pixels is $\log \text{EM} = 27.00 \text{ cm}^{-5}$. The umbral distributions in temperature and emission measure are not as wide as the penumbral distributions. This reflects the fact that sunspot umbrae tend to be more homogeneous than the corresponding penumbrae. The penumbral temperature and emission measure distributions show that the percentage of penumbral pixels with very low temperatures ($T < 1.4$ – 1.5 MK) and very low emission measures ($\log \text{EM} < 26.3$ – 26.4) is not significantly different from the percentage of umbral pixels with such low temperatures and emission measures. This group of penumbral pixels generally occurs in the far leading parts of the penumbrae of leader spots. The penumbral temperature histogram shows a high-temperature tail ($T > 3$ MK) that contains the pixels associated with active region loops that enter the sunspot atmosphere. The same group of pixels can be seen in the emission measure histogram (note the secondary peak around $\log \text{EM} = 27.15$ – 27.20). It is interesting that only 2% of the umbral pixels have temperatures higher than 3 MK and only 10% have emission measures higher than 27.15.

For comparison, in Figure 3 we also show the temperature and emission measure distributions of quiet-Sun areas that were selected from the same full-disk SXT images that were used for the computation of the sunspot plasma parameters that appear in Table 1. For each day, a 128×128 pixel area of quiet Sun was selected. The quiet-Sun plasma parameters were computed after we summed images that spanned about 8 hr and averaged signals from 4 pixels in order to improve the signal-to-noise ratio. The histograms were produced taking into account all 10 days and considering only the pixels with errors $d \log T_e < 0.07$ and $d \log \text{EM} < 0.25$. They show a peak in the quiet-Sun temperature at 1.3 MK and a peak in emission measure at $\log \text{EM} = 26.41$ in good agreement with previous studies (e.g., see the quiet-Sun plasma parameters derived by Krucker et al. 1997). Previous studies have shown that the SXT can measure such low temperatures (e.g., Yoshida et al. 1995 used only one pair of Al.1/AlMg images and derived temperatures at the footpoints of loop structures as low as 1–1.5 MK with error bars less than 0.3 MK). Overall, the sunspot plasma parameters appear higher than the quiet-Sun plasma parameters. Only 2% of the umbral pixels and 3% of the penumbral pixels have temperatures below 1.3 MK, and only 11% of the umbral pixels and 10% of the penumbral pixels have the logarithms of their emission measures below 26.41.

An interesting issue is the properties of the relatively high-temperature, high emission measure pixels of the sunspots with respect to the rest of the active regions. Unfortunately, the quality of the SXT temperature and emission measure images is such that in most cases we were not able to determine a “sunspot loop” criterion as in Brynildsen et

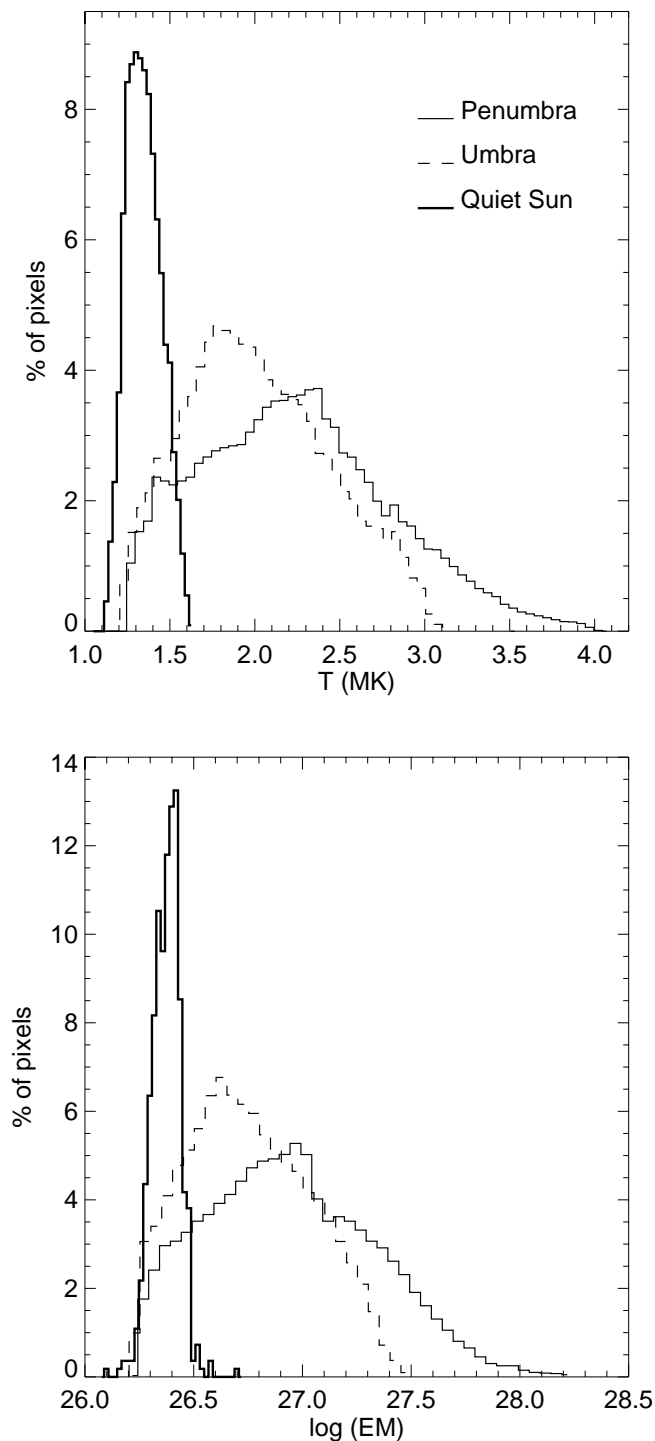


FIG. 3.—Histograms of the distribution of the temperature and emission measure above the umbrae (*dashed lines*) and the penumbrae (*solid lines*). Only pixels from the sunspots that have been presented in the previous figures were used. The vertical axes denote percentage of the total number of umbral or penumbral pixels. For comparison, we give histograms of the temperature and emission measure distribution of quiet-Sun regions (*thick lines*; see text for details). For both sets of histograms we did not take into account pixels with errors due to photon statistics higher than $d \log T_e > 0.07$ and $d \log EM > 0.25$.

al. (1999). Instead, for each sunspot we computed the average temperature of the pixels with the 20% highest temperatures and the average emission measure of the pixels with the 20% highest emission measures. These quantities

were compared with the average temperature and emission measure of the active region and with the average temperature and emission measure of the pixels with the 20% highest temperatures and the 20% highest emission measures in the active region. The results are presented in Table 2. Even the highest sunspot temperatures and emission measures are lower than the average active region temperatures and emission measures (and of course lower than the maximum active region values of the plasma parameters). This result suggests that the active region soft X-ray loops that connect to the sunspot atmosphere are low-temperature, low-density loops.

4. 17 GHz EMISSION ABOVE SUNSPOTS

Contour plots of the 17 GHz emission above the sunspots in total intensity I and circular polarization V appear in Figure 1. For each sunspot, we create the R and L maps and identify which one is appropriate to e -mode (which in all cases is the brightest polarization). In Table 3, we give the maximum brightness temperature in the e -mode map for each sunspot source and its location with respect to the white-light image. We also give the average soft X-ray temperature and density at the location of the radio peak. The density was computed from the emission measure assuming a line-of-sight depth equal to the typical dimension of the radio source. Our densities are subject to additional uncertainties because we cannot estimate the line-of-sight depth directly (limb observations are needed, e.g., see Schmahl et al. 1982). We note, however, that, if instead of the size of the radio sources we use the scale length of the magnetic field along the line of sight (see below) for the density calculations, we find similar results (within 10%–20%). The densities in Table 3 are somewhat smaller than typical active region densities reported in the literature (for a direct comparison between our densities and densities reported in older papers, we must multiply our values by a factor of 2 to compensate for the different abundances used in the emission measure computations). The fact that the derived densities are low is not surprising because only the soft X-ray material was used in the calculations.

In Table 3, we also check the relative contribution of free-free mechanism to the sunspot 17 GHz emission. We computed the expected 17 GHz free-free brightness temperatures from the soft X-ray electron temperatures and emission measures above the microwave sunspot sources (see Dulk 1985 for the formula). Four sunspots of our sample were also observed with the Extreme Ultraviolet Imaging Telescope (EIT). EIT temperature and emission measure maps were computed using the two-temperature component analysis developed by Zhang, White, & Kundu (1999). Since the SXT is not sensitive to very cool plasmas, we added the expected 17 GHz free-free brightness temperature from the average EIT cool component sunspot plasma parameters to the brightness temperatures expected from the soft X-ray emission. The contribution of the EIT cool material is 1092 K. Finally, a brightness temperature of 10,000 K was added to the resulting numbers (the Nobeyama calibration assumes that the brightness temperature of the optically thick chromospheric material is 10,000 K). The expected free-free emission is about 11,260–11,670 K, and it is much lower than the maximum e -mode peaks of most sunspot-associated sources. The narrow range of predicted free-free brightness temperatures reflects the fact that the contribution of the soft X-ray-emitting material is very

TABLE 2
SUNSPOT VERSUS ACTIVE REGION PLASMA PARAMETERS

Date	$T_e^{\text{sunsp a}}$ ($\times 10^6$ K)	$T_{e,\text{ar,aver b}}$ ($\times 10^6$ K)	$T_{e,\text{ar,bright c}}$ ($\times 10^6$ K)	$\log EM_{\text{sunsp d}}$ (cm^{-5})	$\log EM_{\text{ar,aver e}}$ (cm^{-5})	$\log EM_{\text{ar,bright f}}$ (cm^{-5})
1992 Jul 12	3.0 ± 0.18	3.6 ± 0.22	4.2 ± 0.25	27.70 ± 0.19	27.80 ± 0.25	28.67 ± 0.29
1992 Aug 9	2.1 ± 0.15	26.90 ± 0.10
1992 Nov 10	3.5 ± 0.17	3.7 ± 0.25	5.6 ± 0.29	27.91 ± 0.17	27.98 ± 0.22	28.72 ± 0.25
1992 Dec 23	2.4 ± 0.19	3.5 ± 0.21	6.1 ± 0.38	27.08 ± 0.21	28.50 ± 0.24	28.32 ± 0.31
1993 Feb 10	2.2 ± 0.12	2.7 ± 0.17	3.2 ± 0.24	27.02 ± 0.15	27.90 ± 0.19	28.16 ± 0.21
1993 Jun 29	3.7 ± 0.20	4.4 ± 0.27	5.3 ± 0.35	27.28 ± 0.18	27.99 ± 0.24	28.34 ± 0.22
1993 Jul 1	3.5 ± 0.22	3.9 ± 0.28	4.3 ± 0.32	27.37 ± 0.22	27.92 ± 0.21	28.29 ± 0.27
1993 Jul 22	3.3 ± 0.23	3.6 ± 0.20	5.4 ± 0.36	27.60 ± 0.18	27.81 ± 0.20	28.51 ± 0.25
1993 Nov 5	2.3 ± 0.18	3.4 ± 0.24	5.1 ± 0.29	26.81 ± 0.23	28.03 ± 0.28	28.39 ± 0.33
1998 Jun 9	2.8 ± 0.13	26.73 ± 0.18

^a Average temperature of the sunspot pixels with the 20% highest temperatures.

^b Average active region temperature.

^c Average temperature of the active region pixels with the 20% highest temperatures.

^d Average emission measure of the sunspot pixels with the 20% highest emission measures.

^e Average active region emission measure.

^f Average emission measure of the active region pixels with the 20% highest emission measures.

small (only 170–600 K). The 1992 August 9 sunspot (see Fig. 1, row b) shows the lowest e -mode maximum brightness temperature (20,000 K). The fact that the 17 GHz emission above that sunspot is unpolarized confirms that gyroresonance emission is weak and a significant part of its emission comes from the free-free mechanism.

In all other sunspots the peak e -mode T_b is 6–180 times larger than the expected free-free emission, and therefore the gyroresonance mechanism dominates. It has been established (e.g., Vourlidis, Gary, & Shibasaki 1997) that the 17 GHz gyroresonance emission comes from the third harmonic of the gyrofrequency. The fourth harmonic may play some role in sunspots very close to the limb (see White & Kundu 1997). However, such sunspots have not been included in our database. Gyroresonance from the third harmonic means that the photospheric magnetic field is strong enough to bring the 2000 G layer in the low corona/transition region. Such high coronal magnetic fields have been reported previously (e.g., Akhmedov et al. 1986;

White, Kundu, & Gopalswamy 1991; Alissandrakis et al. 1993). Here we note that the KPNO magnetograms suffer from saturation and give only lower limits to the high photospheric magnetic fields (Alissandrakis, Kundu, & Lantos 1980; Nindos et al. 1996; Lee et al. 1997). In Table 3, we give the maximum sunspot magnetic field strengths from Mount Wilson images. The Mount Wilson magnetograms do not saturate, but their spatial resolution is lower than that of the KPNO magnetograms. The reader should treat the magnetic field strengths in Table 3 cautiously because they give only the longitudinal component of the magnetic field while the necessary condition for the emission of third harmonic g-r radiation is that the *total* magnetic field in the low corona should be 2000 G.

An additional feature of the sunspot sources that shows that their emission comes from the g-r mechanism is their high degree of polarization, ρ_c ; the maximum value of ρ_c ranges from 70% to 99.6%. The lowest ρ_c is associated with the 1993 March 9 source, which shows coronal brightness

TABLE 3
FREE-FREE AND GYRORESONANCE EMISSION ABOVE SUNSPOTS

Date	Temperature ^a ($\times 10^6$ K)	Density ^a ($\times 10^9 \text{ cm}^{-3}$)	B_{max} (G)	$T_b^{e\text{-mode}}$ ($\times 10^3$ K)	ρ_c^b (%)	T_b^{f-f} ($\times 10^3$ K)	θ^c (deg)	Location NoRH
1992 Jul 12	2.1 ± 0.19	0.87 ± 0.32	2600–3000	701	98	11.4	33	P
1992 Aug 9	1.8 ± 0.15	0.80 ± 0.26	2100–2500	20	...	11.3
1992 Nov 10	3.5 ± 0.17	1.26 ± 0.41	2100–2500	507	88	11.6	15	P
1992 Dec 23	1.7 ± 0.15	0.98 ± 0.36	2860–3000	311	97	11.6	29	U/P
1993 Feb 10 ^d	2.0 ± 0.12	0.98 ± 0.41	2100–2500	585	94	11.5	26	U
1993 Feb 10 ^e	2.1 ± 0.15	0.88 ± 0.37	2100–2500	141	86	11.4	20	P
1993 Jun 29	1.7 ± 0.11	0.76 ± 0.39	2600–3000	255	93	11.3	28	U
1993 Jul 1	2.3 ± 0.16	0.78 ± 0.44	2600–3000	409	87	11.3	26	U
1993 Jul 22	3.1 ± 0.18	1.20 ± 0.46	2100–2500	112	98	11.6	13	P
1993 Nov 5 ^e	1.7 ± 0.13	0.61 ± 0.28	2100–2500	98	95	11.3	23	U
1998 Jun 9	2.4 ± 0.14	0.67 ± 0.21	2950–3000	268	98	11.3	22	P

NOTE.—U and P denote umbra and penumbra sources, respectively.

^a At the location of the gyroresonance source.

^b Degree of circular polarization at the location of maximum brightness temperature.

^c The angles between the magnetic field and the line of sight needed to reproduce the radio peak if we take into account the plasma parameters.

^d Eastern sunspot.

^e Western sunspot.

temperatures. This means that, with the possible exception of the 1993 March 9 sunspot, practically no o -mode emission contributes to the I peaks.

The peak of the e -mode emission of most sunspot g-r sources lies between 1 and 9×10^5 K. There are two cases with $T_b > 10^6$ K (the 1992 August 17 and the 1993 March 9 sunspots) and three cases with maximum brightness temperatures below 10^5 K. The group of sunspot sources with $T_b < 10^5$ K includes the sources with the lowest dimensions in our data set; their typical average size is lower than $17''$. This may suggest that the effective radio resolution affects the observed brightness temperatures. This is the so-called beam dilution problem, and Vourlidis, Gary, & Shibasaki (1997) showed that indeed this effect plays a role particularly for the small Nobeyama g-r sources. We compared our maps made within AIPS with a beam size of $12''$ with the maps produced with the Nobeyama software (it utilizes the "Steer CLEAN" deconvolution algorithm; Steer, Dewdney, & Ito 1984; Koshiishi 1996) with a beam size of about $17''$ and derived similar conclusions: the brightness temperature of our maps was always higher than the brightness temperature of the corresponding snapshot "Steer CLEAN" maps by a factor of 1.8–4.4. Interestingly, most of our g-r sources with $T_b < 100,000$ K did not appear at all in the "Steer CLEAN" maps. The question that arises now is whether there are additional factors (apart from beam dilution) that may contribute to the low T_b . We note that the parameters of the soft X-ray-emitting material above the sunspots associated with the low- T_b sources are not significantly different from the X-ray plasma parameters of sunspots with stronger g-r sources. Lower angles θ may also contribute to the observed lower brightness temperatures. In most cases the g-r sources with low T_b are associated with sunspots that have the smallest umbrae of the database. We measured the umbrae areas in the white-light images and found that the umbrae of those sunspots were about 1.5–2.5 times smaller than the average umbrae of the rest of the sunspots. Therefore, it is more likely that these sunspots have smaller magnetic field scale length.

For each sunspot that had reliable soft X-ray plasma parameters, we inserted the average temperature and density at the location of the I peak into the formula of g-r opacity. The scale lengths of the magnetic field along the line of sight, L_B , were computed analytically using a dipole magnetic field model. For each sunspot we used the Mount Wilson maximum magnetic field strength and required that the depth of the dipole be such that the radius for the third harmonic gyroresonance surface for 2000 G (i.e., the distance from the center of the umbra at which this surface drops below the corona) matched the observed radius in the 17 GHz sunspot sources. Our calculations show that $L_B = 1.1\text{--}1.9 \times 10^9$ cm. The computed angles θ between the line of sight and the magnetic field required to reproduce the observed e -mode peaks are presented in Table 3; angles between 13° and 40° are needed. Such values are plausible for sunspots near the center of the disk.

For each sunspot for which reliable measurements existed we plotted the average temperature and emission measure above the g-r source as a function of the maximum radio brightness temperature (see Fig. 4). The plots show no overall correlation between the peak T_b and the values of the plasma parameters. This is not surprising because we know that g-r opacity depends more weakly on the plasma parameters than on the magnetic field. Figure 4 also shows

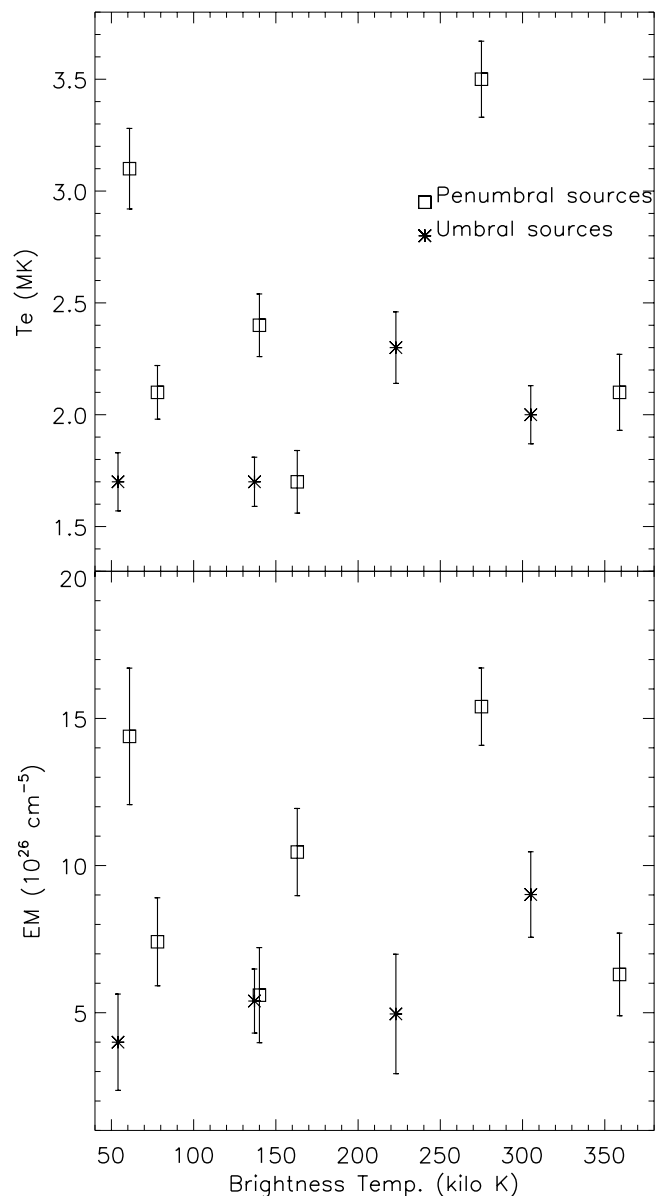


FIG. 4.—Average (top) soft X-ray temperature and (bottom) emission measure at the location of the gyroresonance peak as a function of the maximum brightness temperature of the I map. The asterisks show 17 GHz sources with peaks above the umbra and the squares show 17 GHz sources with peaks above the penumbra.

that the g-r sources that are located above the penumbrae tend to occur in areas with higher temperatures and densities than the g-r sources that are located above the umbrae. This result is due to the fact that the umbral pixels are usually associated with the lowest temperatures and emission measures while in the penumbrae the plasma parameters can be higher because of the penetration of hotter and denser active region material in their atmospheres.

Figure 1 shows that in some sunspots the microwave peak lies above the umbra and in some others above the penumbra. The possible reasons that the peak of a microwave source appears above the penumbra are (1) the existence of currents that twist the magnetic field lines and elevate coronal field strengths above the values expected from simple potential field extrapolations of surface measurements (e.g., Alissandrakis & Kundu 1984; Nindos et al. 1996; Lee et al. 1997) and (2) since g-r absorption depends

on the plasma parameters, local enhancements of the electron temperature and/or density may play the most important role in the shift of the microwave peak away from the umbra even in cases when the magnetic field above the sunspot is potential (i.e., current free). The question of whether the higher plasma parameters above the penumbrae are the primary factor for the appearance of the peak g-r sources there cannot be answered easily because g-r emission is very sensitive to the angle θ and therefore line-of-sight effects and loop inclinations will tend to move the radio peak around. Furthermore, the size of the 17 GHz sunspot sources and the resolution of the NoRH do not allow us to derive solid conclusions. However, a simple method to check the existence of currents above the sunspots is as follows. After rotating the KPNO magnetogram to the time of the 17 GHz image, we find the heliographic coordinates l and b of the point with the maximum magnetic field. We assume radial field lines and a height r of 3000 km for the gyroresonance source. Then we transform the three-dimensional heliographic coordinate system (l, b, r) into image coordinates on the plane of the sky (x, y, z) and compare x and y with the location of the 17 GHz peak. In the sunspots with g-r peak above the umbra the average shift was about $4''$ – $8''$, while for the sunspots whose 17 GHz maxima were above the penumbra the shift was systematically larger (about $10''$ – $15''$). This result suggests that, in the sunspots with penumbral microwave peaks, the twist of the magnetic field lines is larger and currents may play a more important role than in the sources with peaks above the umbra.

5. CONCLUSIONS

In this paper we studied the soft X-ray and 17 GHz emission above a large data set of stable, large sunspots. Our survey confirmed the well-known fact that there is a depression in the soft X-ray emission above sunspots. After subtraction of scattered light, we found that the average sunspot soft X-ray emission in the Al.1 filter images is 15 – 190 DN s^{-1} , while typical values for the bright active region loops of our data set are 500 – 4000 DN s^{-1} . On the other hand, quiet-Sun regions showed intensities of 10 – 50 DN s^{-1} . We note that the distribution of soft X-ray intensity above sunspots is not uniform. In the Al.1 filter images there are very dark pixels with intensities even below quiet-Sun intensities. Although care was taken to avoid sunspots close to the limb, there are also much brighter pixels (which show intensities as high as 75 – 530 DN s^{-1}) presumably associated with loops that connect to the sunspots. Usually the darkest pixels were located above the umbra or the leading part of the penumbra, while the brighter pixels were located in most cases above the following part of the penumbra. This distribution reflects the fact that most of the sunspots of our data set were located at the leading part of the active region.

One primary goal of this research was the systematic, accurate determination of the soft X-ray temperatures and emission measures above sunspots. For sunspots where the majority of their pixels showed uncertainties below $d \log T = 0.07$ and $d \log EM = 0.25$ (which biases the results toward brighter sunspots), we found that the mean temperature of the umbral pixels was 1.8×10^6 K and the mean temperature of the penumbral pixels was 2.4×10^6 K. The mean umbral and penumbral emission measures were $\log EM = 26.60$ cm $^{-5}$ and $\log EM = 27.00$ cm $^{-5}$, respec-

tively. We note that these temperatures are not the lowest temperatures ever reported in active regions with the Al.1/AlMg filters. For example, Yoshida et al. (1995) measured temperatures as low as 1 – 1.5 MK associated with the foot-points of loop structures. Measurements of such low temperatures are possible when we use the combination of Al.1 and AlMg filters (see § 1). Previous studies with the Al.1/AlMg filters sometimes report active region temperatures relatively close to the ones that we derived for the sunspots (Hara et al. 1992; Brosius et al. 1997), but more often average temperatures of about 3.5 MK have been found (e.g., Klimchuk & Gary 1995). In any case, we want to emphasize that for our data set the sunspots always contained the lowest temperatures and emission measures in the active regions.

We consider the derived sunspot plasma parameters as upper limits because (1) in most of the sunspots for which we could not derive reliable plasma parameters, the percentage of dark pixels was higher than in the sunspots that we presented in the figures. Therefore, at least their emission measure should be lower; and (2) in § 2, we explained that the maximum entropy method (MEM) did not work in all cases; in the cases that did not work we subtracted only the scattered light from the far wings of the PSF. Proper MEM deconvolution of the SXT images led to lower temperatures by about 20%, while the resulting temperatures were lower by 11% when only the effect of the far wings was removed from the sunspot images. The deconvolution and/or scattered light subtraction, however, did not affect the emission measures significantly.

A striking feature of the temperature distributions is that the differences between the mean umbral and penumbral parameters are statistically significant. We found that about 10% of the penumbral pixels show temperatures higher than 3 MK and about 26% show emission measures higher than $\log EM = 27.15$. On the other hand, the percentage of umbral pixels with temperatures higher than 3 MK is only 2%, and the percentage of umbral pixels with $\log EM > 27.15$ is only 10%. Therefore, we suggest that the loops associated with the penumbrae are generally hotter and denser than the loops associated with the umbrae. The same conclusion was reached from detailed microwave observations with the VLA (Vourlidas, Bastian, & Aschwanden 1997). We are not the first to suggest that penumbral loops are hotter than umbral loops; this was evident even in early soft X-ray observations (e.g., Harmon et al. 1993). However, it is probably the first time that these differences are quantified. The penumbrae also contain a group of low-temperature, low-density pixels usually associated with their leading parts where the soft X-ray emission is weaker.

The temperatures and emission measures of the brightest sunspot pixels were not only smaller than the temperatures and emission measures of the brightest active region loops but also smaller than the average active region temperatures and emission measures. We note that the plasma parameters that we derived for the brighter part of the active regions are consistent with previously published values (e.g., Kano & Tsuneta 1996; Porter & Klimchuk 1995). This implies that even the brightest loops that connect to sunspot penumbrae have lower temperature and density than usual active region loops away from sunspots. Overall, the sunspot plasma parameters are higher than the plasma parameters of the quiet Sun. The difference between

the sunspot and quiet-Sun plasma parameters is larger than the maximum error bars that we considered and therefore is physically significant.

The coronal radiative energy loss rate above umbrae was calculated using the formula

$$F_r = EM_\nu P(T), \quad (1)$$

where EM_ν is the volume emission measure (in units of cm^{-3}) and $P(T)$ is the radiative loss function of a plasma of temperature T . The emission measures presented in the tables are essentially the volume emission measures divided by the area of the SXT FFI pixel. Therefore, in order to convert our emission measures to EM_ν , we multiplied them by a factor of $(4.91 \times 725 \times 10^5)^2 \text{ cm}^2$. The function $P(T)$ was taken from the paper by Landi & Landini (1999), who used a model of coronal elemental abundances similar to ours. Their $P(T)$ computations were done assuming densities $N_e = 10^{10} \text{ cm}^{-3}$. Of course we did not derive such high densities for our sunspots, but Landi & Landini (1999) show (see their Fig. 5) that the differences between the $P(T)$ computed with $N_e = 10^8 \text{ cm}^{-3}$ and the $P(T)$ computed with $N_e = 10^{10} \text{ cm}^{-3}$ are only 2% or less for the temperature range where the SXT is sensitive. In any case, the errors of the other parameters involved in the calculations are higher. Using the average plasma parameters for the sunspot umbrae (§ 3) we get $\log P(T) = -21.58 \text{ ergs cm}^3 \text{ s}^{-1}$ and consequently $F_r = 1.32 \times 10^{22} \text{ ergs s}^{-1}$. For the quiet-Sun plasma parameters (see § 3), we find $\log P(T) = -21.45 \text{ ergs cm}^3 \text{ s}^{-1}$ and hence $F_r = 1.15 \times 10^{22} \text{ ergs s}^{-1}$. If we use typical active region plasma parameters (e.g., the values cited by Klimchuk & Gary (1995): $T = 3.6 \times 10^6 \text{ K}$, $EM = 1.1 \times 10^{28} \text{ cm}^{-5}$; we get this EM value after we divide their emission measures by a factor of 4 to compensate for the different abundances they used), we find $\log P(T) = -22.10 \text{ ergs cm}^3 \text{ s}^{-1}$ and hence $F_r = 1.10 \times 10^{23} \text{ ergs s}^{-1}$. Therefore, the radiative loss rate above sunspots is only 15% higher than above the quiet Sun but a factor of 8.3 smaller than the typical radiative loss rate above an active region. Our data do not allow detailed computations of the conductive loss rates; consequently, our result does not necessarily imply that the heating rate above sunspots is higher than above the quiet Sun. On the other hand, such speculation cannot be ruled out completely because our data set is biased toward the brightest sunspots.

The study of the 17 GHz emission above the sunspots combined with the soft X-ray plasma parameters showed only one case where the microwave emission was free-free. In all other cases the gyroresonance mechanism played the most important role. The g-r emission comes from the third harmonic of the gyrofrequency. The degree of circular polarization of most g-r sources was higher than 90%, suggesting that there was practically no σ -mode emission from the second harmonic. Thus, our study indicates that magnetic fields as strong as 2000 G exist in the corona above most of our sunspots. We note however that our data set is deliberately biased toward big sunspots whose magnetic fields should fall off slowly with height. Vourlidas, Gary, &

Shibasaki (1997) found that only 13% of the active regions between 1992 July and 1994 December showed g-r cores over some part of their disk crossing.

The peak e -mode T_b of most sunspot g-r sources is between 1 and $9 \times 10^5 \text{ K}$. Using the derived soft X-ray sunspot plasma parameters, we were able to reproduce the peak brightness temperatures of the sunspots assuming angles θ between 13° and 40° , which are plausible for sunspots not very close to the limb. However, these values of θ should be considered as lower limits because of the relatively low spatial resolution of our maps, which may affect the observed brightness temperatures. No correlation was found between the maxima of the microwave sources and the temperatures or emission measures at the locations of the g-r sources. This is a direct consequence of the much stronger dependence of g-r opacity on magnetic field than on the plasma parameters.

The peaks of the g-r emission can occur either above the umbra or above the penumbra. The question whether the higher penumbral temperatures and/or densities alone can account for the occurrence of the g-r peaks above the penumbrae and not above the location of the highest photospheric magnetic field cannot be answered without knowledge of the coronal magnetic field. Our data set shows a compelling case of a sunspot whose peak is above the penumbra not because of higher temperatures/densities but because of the existence of currents (the 1998 June 9 sunspot). For the other sunspots, we do have an indirect indication for a possible very important role of currents that twist the field lines and therefore increase θ above the penumbra. For each sunspot we assumed radial field lines and a height of 3000 km for the formation of the g-r source. We calculated the projection of the position of maximum field from a height of 3000 km on the plane of the sky and compared it with the position of the g-r peak. In sunspots with g-r peaks above the penumbra the shifts are higher by almost a factor of 2 than in sunspots with umbral peaks. Overall the differences are higher than the uncertainties associated with the overlays. Multifrequency observations of g-r sources with higher spatial resolution would be valuable because the resolution of Nobeyama maps does not show the fine structure of sunspot-associated sources.

Our study of the soft X-ray plasma parameters above sunspots indicates that future modeling of microwave sunspot sources should relax the assumption of a plane-parallel density. This combined with nonlinear force-free extrapolations of the photospheric magnetic field will result in better agreement between the observations and models.

This research at the University of Maryland was carried out with support from NSF grants ATM 96-12738 and INT 98-19917 and NASA grants NAG5-6257, NAG5-7901, and NAG5-7370. A. N. would like to thank Jie Zhang for valuable discussions and advice concerning EIT data. He also thanks Angelos Vourlidas for giving him the manuscript of his poster paper on sunspot gyroresonance emission. Finally, we thank the referee for his comments, which led to significant improvement of the paper.

REFERENCES

- Akhmedov, Sh., et al. 1986, ApJ, 301, 460
 Alissandrakis, C. E., Gelfreikh, G. B., Borovik, V. N., Korzhavin, A. N., Bogod, V. M., Nindos, A., & Kundu, M. R. 1993, A&A, 270, 509
 Alissandrakis, C. E., & Kundu, M. R. 1984, A&A, 139, 271
 Alissandrakis, C. E., Kundu, M. R., & Lantos, P. 1980, A&A, 82, 30
 Brosius, J. W., & Holman, G. 1989, ApJ, 342, 1172
 Brosius, J. W., et al. 1997, ApJ, 477, 969
 Brynildsen, N., Maltby, P., Brekke, P., Haugan, S. V. H., & Kjeldseth-Moe, O. 1999, Sol. Phys., 186, 141
 Dulk, G. A. 1985, ARA&A, 23, 169

- Feldman, U. 1992, *Phys. Scr.*, 46, 202
 Gelfreikh, G. B., & Lubyshev, B. I. 1979, *Soviet Astron.*, 23, 316
 Golub, L., Noci, G., Poletto, G., & Vaiana, G. S. 1990, *Nature*, 344, 842
 Gopalswamy, N., Raulin, J.-P., Kundu, M. R., Hildebrandt, J., Krüger, A., & Hofman, A. 1996, *A&A*, 316, L25
 Hara, H., Tsuneta, S., Acton, L. W., Bruner, M., Lemen, J. R., & Ogawara, Y. 1994, *PASJ*, 46, 493
 Hara, H., et al. 1992, *PASJ*, 44, L135
 Harmon, R., Rosner, R., Zirin, H., Spiler, E., & Golub, L. 1993, *ApJ*, 417, L83
 Jahn, K. 1992, in *Sunspots: Theory and Observations*, ed. J. H. Thomas & N. O. Weiss (Dordrecht: Kluwer), 112
 Kano, R., & Tsuneta, S. 1996, *PASJ*, 48, 535
 Klimchuk, J. A., & Gary, D. E. 1995, *ApJ*, 448, 925
 Koshiishi, H. 1996, Ph.D. thesis, Univ. Tokyo
 Krucker, S., Benz, A. O., Bastian, T. S., & Acton, L. W. 1997, *ApJ*, 488, 499
 Krüger, A., Hildebrandt, J., & Fürstenberg, F. 1985, *A&A*, 143, 72
 Kundu, M. R., Alissandrakis, C. E., Bregman, J. D., & Hin, A. C. 1977, *ApJ*, 213, 278
 Landi, E., & Landini, M. 1999, *A&A*, 347, 401
 Lee, J., McClymont, A. N., Mikić, Z., White, S. M., & Kundu, M. R. 1998, *ApJ*, 501, 853
 Lee, J., White, S. M., Gopalswamy, N., & Kundu, M. R. 1997, *Sol. Phys.*, 174, 175
 Martens, P. C., Acton, L. W., & Lemen, J. R. 1995, *Sol. Phys.*, 157, 141
 Meyer, J.-P. 1985, *ApJS*, 57, 173
 Nakajima, H., et al. 1991, *Proc. IEEE*, 82, 705
 Nindos, A., Alissandrakis, C. E., Gelfreikh, G. B., Kundu, M. R., Dere, K. P., Korzhavin, A. N., & Bogod, V. M. 1996, *Sol. Phys.*, 166, 55
 Nindos, A., Kundu, M. R., White, S. M., Gary, D. E., Shibasaki, K., & Dere, K. P. 1999, *ApJ*, 527, 415
 Pallavicini, R., Vaiana, G. S., Tofani, G., & Felli, M. 1979, *ApJ*, 229, 375
 Porter, L. J., & Klimchuk, J. 1995, *ApJ*, 454, 499
 Sams, B. J., Golub, L., & Weiss, N. O. 1992, *ApJ*, 399, 313
 Schmahl, E. J., Kundu, M. R., Strong, K. T., Bentley, R. D., Smith, J., Jr., & Krall, K. 1982, *Sol. Phys.*, 80, 233
 Steer, D. G., Dewdney, P. E., & Ito, M. R. 1984, *A&A*, 137, 159
 Tsuneta, S., et al. 1991, *Sol. Phys.*, 136, 37
 Vourlidas, A., Bastian, T. S., & Aschwanden, M. J. 1997, *ApJ*, 489, 403
 Vourlidas, A., Gary, D. E., & Shibasaki, K. 1997, *BAAS*, 29, 01.34
 Walker, A. B. C., Barbee, T. W., Hoover, R. B., & Lindblom, J. F. 1988, *Science*, 241, 1781
 Webb, D. F., & Zirin, H. 1981, *Sol. Phys.*, 69, 99
 White, S. M. 1999, *Sol. Phys.*, 190, 309
 White, S. M., & Kundu, M. R. 1997, *Sol. Phys.*, 174, 31
 White, S. M., Kundu, M. R., & Gopalswamy, N. 1991, *ApJ*, 366, L43
 White, S. M., Thomas, R., Brosius, J. W., & Kundu, M. R. 2000, *ApJ*, in press
 Yoshida, T., Tsuneta, S., Golub, L., Strong, K., & Ogawara, Y. 1995, *PASJ*, 47, L15
 Zhang, J., White, S. M., & Kundu, M. R. 1999, *ApJ*, 527, 977
 Zirin, H. 1988, *Astrophysics of the Sun* (Cambridge: Cambridge Univ. Press)